Composite Structures 401 (2027) 121032

Contents lists available at ScienceDirect

Composite Structures

journal homepage: www.elsevier.com/locate/compstruct

Application of integrated epoxy electrically insulated piezoresistive carbon fiber sensors in strain sensing of CFRP structures

Maximilian Korff, Tobias Dickhut *

University of the Bundeswehr Munich, Werner-Heisenberg-Weg 39, Neubiberg, 85579, Germany

ARTICLE INFO

Keywords:
Structural health monitoring
Carbon fiber sensing
Non-destructive testing
Component-integrated strain sensors

ABSTRACT

Integrated strain sensing in CFRP using piezoresistive carbon fiber sensors (CFS) is hindered by leakage currents and signal interference caused by laminate conductivity, while thermoset-compatible insulation concepts validated in tensile tests remain scarce. This work introduces an insulated carbon fiber sensor (iCFS) concept intended to provide an approximately linear strain-dependent resistance response in CFRP. The iCFS are fabricated by twisting and pretensioning 1 K carbon rovings, epoxy impregnation, dip coating, and four-wire contacting. Insulation quality is assessed in liquid gallium, and the sensors are embedded in autoclave-processed unidirectional (UD) CFRP and GFRP laminates and characterized by cyclic tensile tests using video-extensometer reference strains. Fully insulated iCFS retain >99.8% of their initial resistance in gallium. For three specimens per material system, five measurements of five load–unload cycles each were performed at target strains of 0.2% and 0.6%. A single fit was applied to each five-cycle measurement, yielding specimen-specific mean gauge factors of 1.64–2.12. In one exploratory increasing-load test per material system, a more pronounced nonlinear response emerged at approximately 0.7% strain in the investigated specimens. The results provide proof-of-concept evidence for electrical insulation and iCFS integration in UD CFRP for strain-sensitive resistance measurements under controlled room-temperature axial tensile loading.

1. Introduction

Modern composite structures are increasingly being used in high-performance applications, from aerospace components to gaseous and cryogenic fuel tanks, owing to their exceptional strength-to-weight ratios and design flexibility [1]. As the complexity and safety demands of these structures grow, integrated structural health monitoring has become essential [2]. In particular, the in situ measurement of strain is crucial for assessing the integrity and lifetime of composite components. Carbon fibers, with their high electrical conductivity and mechanical robustness, present a promising route for realizing integrated sensors that can continuously monitor strain within composite materials [3,4]. While carbon fibers or graphene-coated glass fibers [5] have been successfully employed as sensor elements in glass-fiber-reinforced plastics (GFRP), where the inherent electrical insulation of the matrix and insulating glass fibers facilitates accurate measurements [6–10], their direct application in carbon-fiber-reinforced plastics (CFRP) is considerably more challenging. In CFRP, the conductive nature of the composite material can interfere with the sensor's signal, necessitating an effective electrical insulation strategy for the carbon fiber sensors (CFS) [11,12]. Conventional sensor technologies, such as fiber Bragg gratings, offer high sensitivity but often involve complex, costly setups and are vulnerable to fiber breakage during handling, especially when routed out of the component [13]. In addition, the strain behavior of CFRP can also be measured through resistive measurements of the CFRP laminate itself [14,15], also using a neural network for calibration [16,17].

It should be noted that the measured resistances and the measurement behavior strongly depend on the orientation of the layers in the component [14,15]. For piezoresistive measurements using specific conductive sensor fibers, GFRP layers can be used as insulating layers to prevent leakage currents through the CFRP [18]. [18] also summarizes the various known fields of application and the piezoresistive measurement of unidirectional GFRP and CFRP laminates and compiles the variables required for the calibration of different prepregs and fibers without referring to electrically insulated piezoresistive sensor fibers measured in CFRP.

Recent research has explored several approaches to address the challenges of piezoresistive strain sensing in electrically conductive CFRP structures.

Using thermoplastic 3D printing [19–22], insulated carbon fiber components can be manufactured, enabling strain measurement

* Corresponding author.
E-mail address: tobias.dickhut@unibw.de (T. Dickhut).

https://doi.org/10.1016/j.compstruct.2026.121032
Received 15 January 2026; Received in revised form 6 October 2026; Accepted 24 October 2026
Available online 1 November 2026
0263-8223/© 2026 The Authors. Published by Elsevier Ltd. This is an open access article under the CC BY license (http://creativecommons.org/licenses/by/4.0/).
Open access funding enabled and organized by Projekt DEAL.

through the component. Superficial bonding of conductive nanotube fibers on CFRP also provides the necessary insulation for piezoresistive sensors [23,24]. A different approach is the insulation of the carbon sensor fiber using a cotton textile [25,26]. This requires a comparatively bulky insulation layer, which increases the influence on the CFRP component. In [27], a thermoplastic insulation coating for carbon fibers and carbon nanotubes is described for use in the in vivo detection of dopamine. However, integration into composite laminates and a strain sensing test is not performed. In addition, these methods do not offer the possibility of integrated contacting of the sensor fiber to a copper cable, which is essential for a locally limited strain measurement. In addition, because the insulation is made of a thermoplastic material, questions remain regarding material compatibility and creep for use in a thermoset matrix. In [28], carbon fiber sensors (CFS) are incorporated into thermoplastic textiles using warp-knitting techniques, enabling electrically insulated strain measurements, as further demonstrated in [29]. This also requires large-scale insulation layers.

In [30], carbon nanotubes insulated with a thermoplastic coating are presented, offering promising diameters for sensing applications. However, these were tested without integration into structural components for tensile testing and after integration into CFRP for a three-point bending test. Furthermore, no method for contacting the sensors to copper wiring within the component is proposed.

The reviewed literature indicates a lack of reliable electrical insulation methods for piezoresistive carbon yarn sensors and an insufficient validation of strain measurement data obtained from tensile tests with sensors integrated into CFRP.

This paper addresses this gap by introducing insulated carbon fiber sensors (iCFS). These sensors utilize a novel duromeric insulation process for carbon yarn and a multi-layer epoxy-based dip-coating method. The process combines a multi-layer epoxy-based insulation method with pre-tensioning intended to promote an approximately linear strain-dependent sensor response. Its functionality and limitations were evaluated by tensile tests using comparative strain data collected using a video extensometer. UD tensile tests were performed in conductive CFRP laminates as the primary target material system and in insulating GFRP laminates as an electrically non-conductive reference system. The GFRP specimens were used to characterize the strain-dependent electrical response of the embedded iCFS in an electrically insulating laminate environment, thereby avoiding electrical interaction between the sensor and conductive carbon-fiber reinforcement. This reference configuration therefore provides a non-conductive comparison for evaluating the response of the embedded iCFS. In addition, the sensor behavior was evaluated until sensor failure to demonstrate the applicability and limitations of the proposed approach.

2. Materials and methods

The following section describes the materials, sensor preparation steps, and manufacturing processes used for the fabrication and characterization of the multi-layer insulated carbon fiber sensors embedded in composite laminates.

2.1. Materials

The materials used in this study include the base components for sensor fabrication as well as the prepreg systems for the composite laminates. The specific composition and processing compatibility of each material are critical for ensuring proper insulation, sensor integration, and mechanical performance.

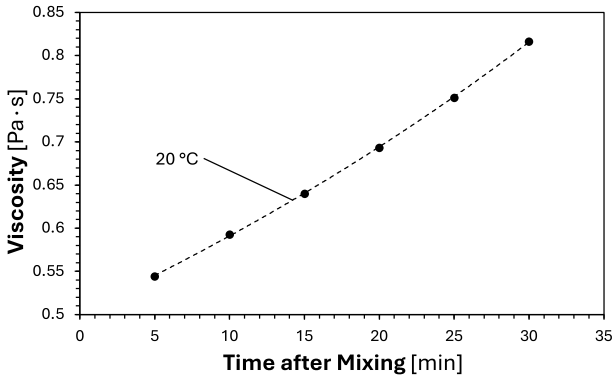


Fig. 1. Viscosity profile of epoxy resin L20 with EPH 161 at 20°C.

2.1.1. Epoxy-insulated carbon fiber sensors

The sensor fibers used in this study were 1 K T300 carbon fiber tows supplied by Toray. For insulation and sensor integration, an epoxy resin system consisting of Epoxy L20 and Hardener EPH 161 (R&G GmbH, Germany) [31] was used. The resin mixture had a measured viscosity of 0.495 Pa·s at 20 °C after one minute of mixing (Fig. 1).

For local insulation of solder joints, a commercially available 5-minute epoxy adhesive (Everglue 2 K 5-minute-epoxy) [32] was applied. Copper wires with a diameter of 0.29 mm were used for electrical connections. Nickel electroplating of the sensor ends was performed using a nickel sulfate electrolyte bath as described in [33].

2.1.2. CFRP and GFRP laminates with integrated iCFS manufactured using the autoclave process

To produce unidirectional laminate specimens with integrated iCFS, SIGRAPREG G U300-0/NF-E320/35% (SGL Carbon, Germany) with a resin content of 35 wt% was used for GFRP specimens and SIGRAPREG C U230-0/NF-E322/39% (SGL Carbon, Germany) with a resin content of 39 wt% was used for CFRP specimens. According to the manufacturer, both resin systems have identical curing behavior and differ only slightly in their tackiness during processing.

2.2. Manufacturing

2.2.1. Epoxy-insulated carbon fiber sensors

To produce multi-layer insulated CFS (iCFS), an impregnation layer and a thin epoxy resin layer were applied to the sensor (Fig. 2a) for insulation using dip coating.

For this purpose, a pre-impregnated CFS, which already allows measurements in GFRP, was coated with a thin layer by horizontal immersion in epoxy resin. Because the fiber was not withdrawn vertically from the epoxy, unlike in e.g. [34], this process requires precise adjustment of the rheological properties of the resin to enable a continuous and thin-walled coating. The process of sensor production and insulation is described in detail below.

To minimize the influence of the sensors on the stiffness and strength of the laminate, the integration should be as minimally invasive as possible, ideally through an extremely thin insulation layer. Since the sensors are intended for use in load-bearing structures, it is essential to ensure compatibility between the sensor material and the thermosetting resin system of the CFRP. Using the same material system for both the sensor and the component is particularly beneficial, as it helps to minimize material stresses arising, for example, from differences in thermal expansion coefficients. Consequently, the insulation layer should not only be as thin as possible but also belong to the same material group as the CFRP matrix. At the same time, it must be ensured that the layer is thick enough to achieve continuous insulation coverage while limiting the number and extent of local thick spots.

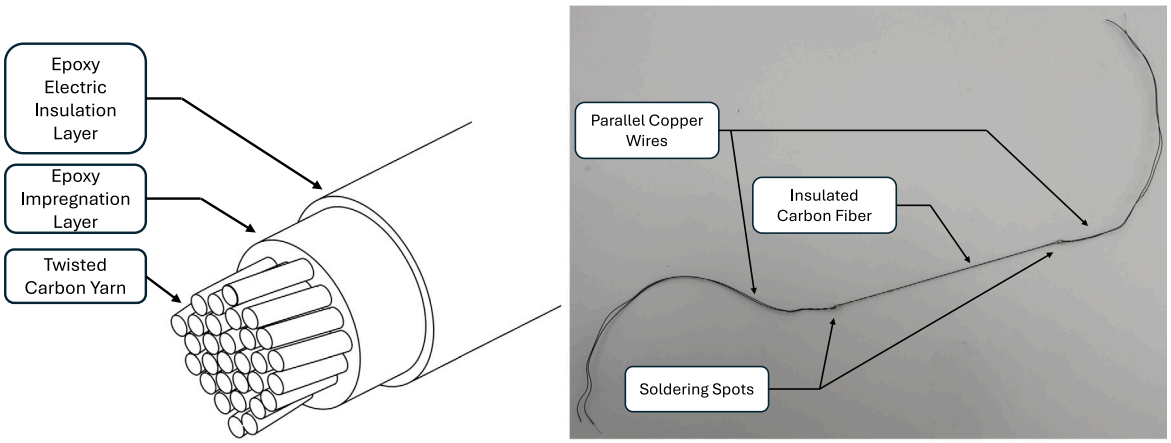


Fig. 2. (a) Schematic drawing of the sensor structure, (b) Manufactured insulated sensor with insulated solder joints connected to two wires on each side.

To promote a more linear strain-dependent response of the iCFS, a defined pre-tension was applied during sensor fabrication based on the considerations reported in [35]. Pre-tensioning can promote uniform fiber alignment and reduce internal variability, thereby potentially contributing to a more consistent piezoresistive response and facilitating sensor calibration.

In contrast, strongly strain-dependent gauge factors were reported in [30] for sensors manufactured without pre-tensioning.

In the present work, the epoxy-based insulation method was therefore combined with the application of a defined pre-tension to reduce potential variability in the sensor response. Sensor preforms were fabricated from 1 K T300 carbon fibers (Toray) with a length of 1 m under a controlled tensile load and twisted at a defined rate of 15 turns per meter. To accomplish this, the carbon fibers were clamped into the fiber holders and twisted the required number of turns (Fig. 3a and b). Since the fibers were clamped in place, the same nominal number of turns could be applied to each fiber. The fibers were then pre-tensioned to approximately 10 N using the tensioning mechanism on one side of the tensioning device. The tensioning process was calibrated using a KERN HCB 50K20 and was performed before every fiber production run. This process was intended to reduce variations in the sensor geometry and contribute to more consistent fitted gauge factors across the investigated strain levels.

The twisted sensor fibers were then impregnated with an initial layer of epoxy resin (Epoxidharz L20, Hardener EPH 161) and pre-cured at room temperature (RT). After pre-curing, the impregnated fibers were cured in an oven at a low heating rate of 5°C per hour and a maximum temperature of 110°C to prevent the resin from flowing and the glass transition temperature of the resin from being exceeded during curing. The preforms were then cut to the required sensor length before the actual production and insulation of the sensors took place. For the experiments described in the following sections, a sensor length of 105 mm was chosen. To attach copper cables to the CFS, the epoxy matrix at the ends of the fiber preforms was removed by selective flame treatment and cleaned with isopropyl alcohol. Subsequently, the exposed carbon fiber ends were electroplated with nickel using the nickel bath composition described in [33] and soldered to thin copper wires with a diameter of $d = 0.29$ mm. To limit the measurement to the length of the carbon fiber, a four-point measurement was performed by soldering two copper cables to each side of the CFS. After soldering the CFS to the test leads, the CFS were insulated to become iCFS in a two-step process.

First, the fibers were coated with an epoxy resin using dip coating at 20°C. The viscosity of the resin, measured one minute after mixing, was 0.495 Pa s. Then the fibers were pre-cured in a vertical orientation. The dip coating was performed by pulling the sensor fiber through a horizontal resin bath, ensuring no contact between the mold and the fiber (see Fig. 3c). The copper wires were routed so that the length pulled through the resin was as short as possible in order to preserve their functionality and minimize resin-induced weight gain. Curing was performed vertically by hanging the copper wires on one side from a horizontal rod of a laboratory stand using adhesive tape. After pre-curing at 20°C, the fibers were post-cured in the oven analogously to the first curing step (see description above).

After post-curing in the oven using the same procedure as in the first curing step, the contact area between the iCFS and the measuring leads was insulated. This was carried out using fast-curing 5-minute epoxy resin. After mixing, the resin was applied to a convex surface and pre-cured for three minutes. The soldered areas of the iCFS were then briefly immersed in the epoxy resin while rotating and pre-cured with continuous rotation until gelation was complete. Complete curing was then performed at room temperature without rotation. An insulated sensor is shown in Fig. 2b.

To quantify the resin uptake after each insulation step, the fiber volume content (FVC) was determined following every coating process. For this purpose, the masses of the unimpregnated fibers and fibers of comparable length after each coating step were measured. The density of the T300 fiber is assumed to be 1.7635 g/cm^3 [36], while the resin density of 1.152 g/cm^3 was determined by hydrostatic weighing according to DIN EN ISO 1183-1 [37]. The FVC is calculated using:

$$FVC = \frac{m_f/\rho_f}{m_f/\rho_f + (m - m_f)/\rho_r} \quad (1)$$

where m_f denotes the average mass of the resin-free fibers, and m represents the mass of the respective insulated fiber. A sample size of $n = 10$ was used for each measurement condition: bare fiber, fiber with impregnation, and fiber with impregnation and insulation. The results are shown in Fig. 8.

2.2.2. CFRP and GFRP laminates with integrated iCFS manufactured using the autoclave process

To produce CFRP and GFRP laminates with integrated iCFS in the autoclave, prepreg layers were cut to size and placed on a polished aluminum plate with a layer of release foil. As the iCFS was embedded in the middle of the laminate, the layers were divided lengthwise in the direction of the sensor as shown in Fig. 4. This allowed the copper cables to be routed out of the laminate. As both the sensors and the solder joint to the copper cable are located inside the component, it is essential that both components are insulated in CFRP. To protect the wires from sticking to the resin of the laminate, the wires were separated with release foil and fixed with tape to prevent shifting in the vacuum bag. To ensure a flow from the laminate to the vacuum line,

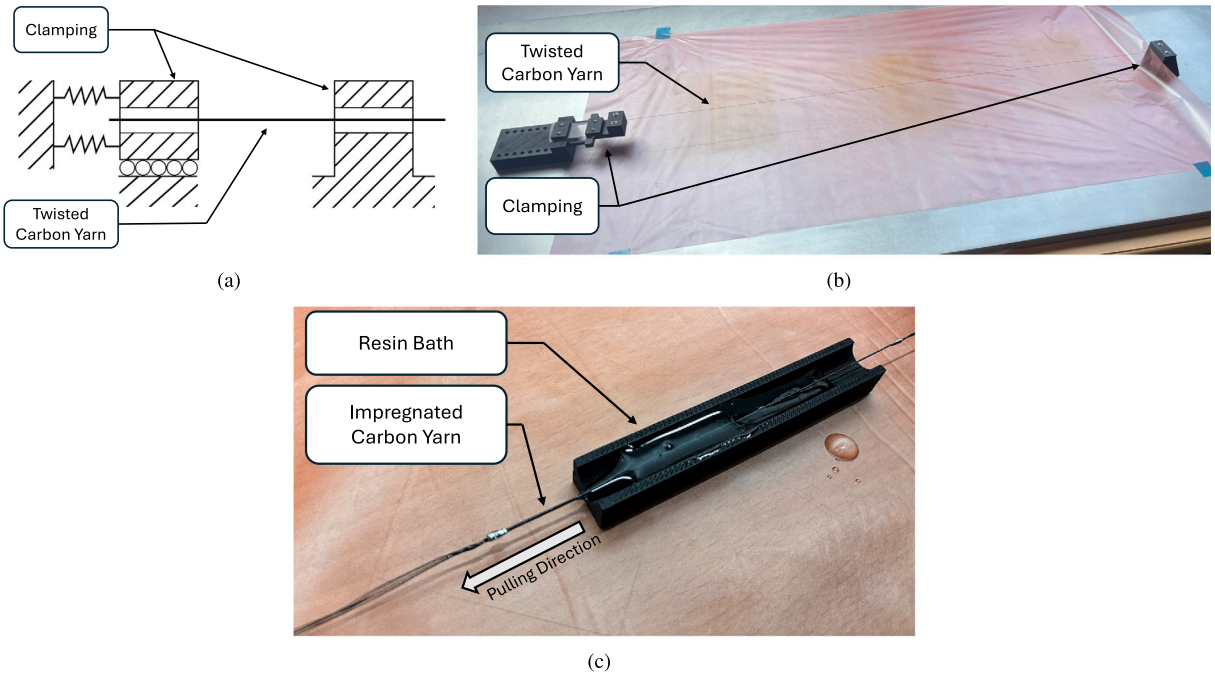


Fig. 3. (a) illustrates the pre-tensioning concept for manufacturing sensor fibers according to [35], (b) illustrates the pre-tensioning device used to manufacture carbon fibers with a defined twist density (twists per meter) under controlled tensile loading conditions. (c) shows the dip coating method to insulate the carbon fiber. The roving was guided through the resin bath, while the copper wires were kept in contact with the resin to the minimum extent possible in order to preserve their functionality and minimize resin-induced weight accumulation.

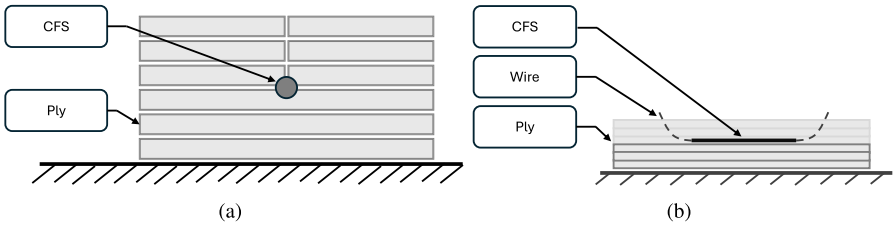


Fig. 4. (a) Frontal cross section of the laminate setup with iCFS sensor. The first 3 of the total of 6 prepreg layers are placed as one sheet. For the upper 3 layers, it is necessary to place two cut-outs side by side with the iCFS in between so that the copper cables can be led out at the top, (b) Lateral cross section of the laminate setup with iCFS sensor. The iCFS is placed on the third layer from the bottom. The copper cable is routed through the layers above.

peel ply was placed at the edges of the laminate. Then an aluminum pressure plate was placed on top of the structure to achieve an even surface on top of the laminate. Afterwards, the setup was covered with breather fleece and a vacuum bag. For curing in the autoclave, a typical curing cycle for the SIGRAPREG GFRP and CFRP prepreg of 90°C for 3 h with an autoclave pressure of 2 bar, a heating ramp of 0.5 °C/min and a vacuum level of 800 mBar was used. Due to the high resin flow of the SIGRAPREG prepreg and the cables of the iCFS, the unpacking process must be carried out with particular care to prevent the cables from coming off. The same applies for gluing the end tabs and cutting the specimens adapted from DIN EN 2561 [38], but with increased sample width of 30 mm as well as a sample thickness of 1.5 mm (Fig. 9a).

2.3. Characterization methods

2.3.1. Sensor insulation test in a conductive Ga bath

To check the quality of the manufactured insulation layer under conditions as close as possible to those of the embedded sample, the sensors were immersed in a bath of elemental gallium at 35°C to ensure the liquid phase of the gallium. The electrical resistance was measured before (R_0) and after immersion (R_{Ga}). By comparing R_0 and R_{Ga}, defects in the insulation layer are detected directly, as insufficiently insulated areas lead to a significant drop in the line resistance. The measurement setup is shown in Fig. 5. An overview of the measured resistances of insulated and uninsulated CFS with a sample size of n = 5 for each condition is shown in Table 1.

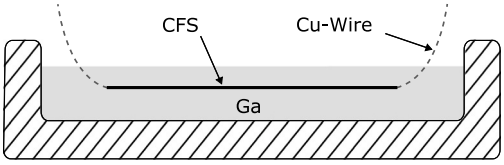


Fig. 5. Setup for testing the insulation properties of the iCFS using a gallium bath.

2.3.2. Piezoresistive properties of insulated iCFS embedded in CFRP and GFRP determined by tensile testing

To determine the gauge factor (k), UD specimens made of CFRP and GFRP with embedded iCFS were cut in accordance with DIN EN 2561 (Section 2.2.2) and loaded to different strain levels (0.2 %, 0.6 %) using a Zwick Z100 universal testing machine (UTM). For each specimen and target strain level, five repeated measurements were performed on the

same embedded iCFS specimen, with each measurement comprising five consecutive load–unload cycles. Thus, the 25 cycles per specimen and strain level represent repeated observations on the same embedded sensor and do not constitute 25 independent specimens or independent sensor replicates. For this purpose, one side of the test surface of the tensile specimens (Fig. 9b) was first coated with white paint for optical strain measurement using a ZwickRoell videoXtens 1C/1H video extensometer. For a homogeneous reference strain measurement, four tracking regions with a size of 128 × 128 pixels were placed centrally along the specimen surface over a gauge length of 50 mm. The strain value obtained from the video extensometer therefore represents an averaged axial reference strain over this gauge length and was used for comparison with the electrical sensor response. The video extensometer, operated in conjunction with the Zwick universal testing machine, recorded strain at 10 Hz, while the electrical resistance was independently recorded at 1 Hz. Prior to testing, the video extensometer was calibrated according to the manufacturer's procedure. According to the manufacturer's specifications, the video extensometer corresponds to accuracy class 1, providing an accuracy of 1 % of the measured value and a displacement resolution of 0.25 µm. The two datasets were matched stepwise and manually using the recorded time information and the identifiable progression of the loading sequence. The matching was performed with reference to the load-reversal points of the cyclic tests, which served as distinct reference points for the temporal alignment of the two datasets. The datasets were subsequently combined at a common sampling frequency of 1 Hz by assigning the corresponding strain value to each resistance measurement. No automated synchronization or additional time-shift correction beyond this manual alignment was applied. Consequently, a residual temporal mismatch and an associated error cannot be excluded, particularly in the vicinity of the load-reversal points. The manual matching was performed over the complete cyclic loading sequence shown in Fig. 12. Since no full-field strain measurement was performed, the optical reference measurement does not provide information on the local strain field in the direct vicinity of the embedded sensor. Consequently, local strain concentrations or strain gradients around damage features, such as the interlaminar crack discussed in Section 3.5, cannot be directly resolved from the optical data. The interpretation of this damage mechanism is therefore based on the combined evaluation of the optical specimen response and the electrical resistance signal.

A fine speckle pattern was then applied with black paint to enable optical tracking. The specimen was subsequently placed in the self-clamping jaws of the tensile testing machine, and the cables were connected to the measuring device, a Rohde & Schwarz HMC8012 multimeter. Subsequently, the strain levels were reached cyclically as described at a machine speed of 5 mm/min. Due to the self-tensioning jaws of the UTM, the elongation between the load phases was reduced to a minimum of 0.02 %, as otherwise there is a risk of the clamping device being released. The strain (ε) was controlled by the video extensometer connected to the UTM. The gauge factor of the iCFS is calculated according to [39] as follows:

$$k = \frac{\Delta R/R_0}{\varepsilon} \tag{2}$$

To determine the gauge factor for each measurement, a single linear least-squares fit was applied to the combined strain ε_i and resistance change RC_i data from five consecutive load–unload cycles, following the method described in [40]. For each specimen and target strain level, five such measurements were evaluated, yielding five fitted gauge factors from which the mean and sample standard deviation (SD) were calculated. The objective function, i.e., the Sum of Squared Errors (SSE), is given by

$$\mathrm{SSE}(\alpha, K) = \sum_i (y_i - (\alpha + K x_i))^2 \tag{3}$$

Since no change in RC is expected in an unloaded system, α can be assumed to be zero due to the curve passing through the origin. This results in the minimization of the formula, where k is the gauge factor from Eq. (2):

$$\mathrm{SSE}(k) = \sum_i (RC_i - (k\varepsilon_i))^2 \tag{4}$$

Differentiating SSE(k) with respect to k and setting the derivative to zero leads to:

$$\frac{d(\mathrm{SSE})}{d\mathrm{k}} = -2\sum_i \varepsilon_i (RC_i - (k\varepsilon_i)) = 0 \tag{5}$$

Solving for k gives the analytical expression for the least-squares estimate of the gauge factor:

$$k = \frac{\sum_i \varepsilon_i \cdot RC_i}{\sum_i \varepsilon_i^2} = \frac{\vec{\varepsilon}^{\mathsf{T}} \cdot \vec{RC}}{\vec{\varepsilon}^{\mathsf{T}} \cdot \vec{\varepsilon}} \tag{6}$$

To quantify the fit quality for each five-cycle measurement, the root mean square error (RMSE) was calculated from the residuals of the relative resistance change with respect to the fitted response according to

$$\mathrm{RMSE} = \sqrt{\frac{1}{n}\sum_{i=1}^{n}\left(RC_i - RC_{\mathrm{fit},i}\right)^2}, \tag{7}$$

where $RC_i = \Delta R_i/R_0$ is the measured relative resistance change, $RC_{\mathrm{fit},i} = k\varepsilon_i$ is the corresponding fitted value, and n denotes the number of data points included in the fit. The RMSE is reported in percentage points (pp) of relative resistance change. In addition, the coefficient of determination was calculated as

$$R^2 = 1 - \frac{\sum_{i=1}^{n}\left(RC_i - RC_{\mathrm{fit},i}\right)^2}{\sum_{i=1}^{n}\left(RC_i - \overline{RC}\right)^2}, \tag{8}$$

where $\overline{RC}$ denotes the mean relative resistance change of the data points included in the fit.

To assess the sensitivity of the fitted gauge factor to residual uncertainty in the temporal alignment of the independently recorded strain and resistance signals, a sensitivity analysis was performed separately for each five-cycle measurement. Given the manual alignment based on distinct load-reversal points and the different sampling rates of the two measurement systems, additional relative time shifts ranging from −0.5 s to +0.5 s in increments of 0.1 s were applied around the nominal alignment ($\Delta t = 0$) to represent a plausible range of residual temporal misalignment. For each investigated time shift Δt_j, the gauge factor $k(\Delta t_j)$ was recalculated using the same least-squares fitting procedure as for the nominal alignment. The absolute relative change in gauge factor for each additional time shift was calculated with respect to the gauge factor at the nominal alignment, $k(0)$, according to

$$\Delta k_{\mathrm{rel},j} = \left|\frac{k(\Delta t_j) - k(0)}{k(0)}\right| \times 100\%, \tag{9}$$

where $k(\Delta t_j)$ denotes the gauge factor obtained for the additional relative time shift Δt_j and $k(0)$ denotes the gauge factor obtained at the nominal alignment. Thus, $\Delta k_{\mathrm{rel},j}$ quantifies the magnitude of the relative change in the fitted gauge factor caused by a given additional temporal shift, irrespective of the direction of the change. For each repeated measurement, the sensitivity metric S_k was then defined as the maximum absolute relative change in gauge factor over all investigated additional time shifts:

$$S_k = \max_{\Delta t_j}\left(\Delta k_{\mathrm{rel},j}\right) = \max_{\Delta t_j}\left|\frac{k(\Delta t_j) - k(0)}{k(0)}\right| \times 100\%. \tag{10}$$

Accordingly, a small value of S_k indicates that the fitted gauge factor is only weakly affected by variations in the temporal alignment within the investigated shift range. For each specimen and investigated strain level, five repeated measurements were performed, with each measurement comprising five consecutive loading–unloading cycles that were evaluated jointly using a single least-squares fit. The sensitivity

analysis was performed independently for each of these five repeated measurements. The resulting five S_k values for each specimen and strain level are reported as mean [maximum] in Table 3.

To enable a qualitative comparison (Fig. 12) of the temporal evolution of the strain and relative resistance-change signals, both quantities are separately normalized to the interval $[0, 1]$ over the respective five-cycle measurement. The normalized strain $\tilde{\varepsilon}_i$ and normalized resistance change $\widetilde{RC}_i$ are calculated using min–max normalization:

$$\widetilde{RC}_i = \frac{RC_i - RC_{\min}}{RC_{\max} - RC_{\min}} \tag{11}$$

$$\tilde{\varepsilon}_i = \frac{\varepsilon_i - \varepsilon_{\min}}{\varepsilon_{\max} - \varepsilon_{\min}} \tag{12}$$

where ε_i is the strain measured using the video extensometer and $RC_i = \Delta R_i / R_0$ is the relative resistance change of the iCFS. The normalized signal deviation (NSD), expressed as a percentage, is subsequently defined as the pointwise absolute difference between the two normalized signals multiplied by 100:

$$\mathrm{NSD}_i[\%] = 100 \left| \tilde{\varepsilon}_i - \widetilde{RC}_i \right| \tag{13}$$

The NSD is used to qualitatively identify the temporal distribution and magnitude of differences between the normalized signal profiles over the loading–unloading cycles. Values close to zero indicate similar normalized signal levels, whereas higher values indicate larger local differences. Since the separate normalization removes differences in signal amplitude and sensitivity, the NSD does not represent a measurement error or independently determined sensor accuracy. Moreover, residual temporal mismatch between the independently recorded signals may contribute to increased NSD values, particularly near the load-reversal points.

To visualize the fitting quality, the fitting deviation (FD_i) is calculated as the signed difference between the measured relative resistance change ($RC_{\mathrm{meas},i}$) and the corresponding fitted value ($RC_{\mathrm{fit},i}$) obtained using Eq. (6):

$$FD_i = RC_{\mathrm{meas},i} - RC_{\mathrm{fit},i} \tag{14}$$

The measurement results for iCFS specimens in GFRP and CFRP composites for 0.2 % and 0.6 % strain are described in Section 3.4 and are shown in Fig. 12.

2.4. Strain capacity evaluation

To characterize the piezoresistive behavior of the iCFS, GFRP and CFRP tensile specimens, analogous to Fig. 9a, were loaded to failure until the iCFS signal was lost. During the measurement, strain was captured using a video extensometer while the iCFS signal was recorded. This enabled the sensor behavior under extreme loading conditions in both CFRP and GFRP to be assessed. The CFRP and GFRP data were compared to examine the sensor response in conductive and non-conductive laminate configurations, particularly at high loads where failure of the insulation layer may become relevant. The exploratory tests were used to identify the strain range at which the resistance responses of the two investigated specimens departed from approximately proportional behavior. The exploratory tests additionally examined whether progressive tensile loading produced identifiable changes in the resistance response. Due to the single-specimen design and the absence of independent damage confirmation, these changes were not interpreted as validated indicators of overload or damage.

3. Results and discussion

3.1. Epoxy-insulated carbon fiber sensor

Thermoset-coated carbon fiber sensors were manufactured using a multi-step approach consisting of producing semi-finished impregnated fiber yarn, soldering to thin copper wires, insulation of the wire and insulating finish at the soldering area. The insulation quality was strongly dependent on the ambient temperature. An ambient temperature of 20°C was essential for uniform and functional insulation. The viscosity curve for this temperature of the resin used, as described in Section 2.1.1, is therefore shown in Fig. 1. Fig. 6 shows three micrographs of cross-sections of iCFS embedded in cold curing epoxy resin taken from three different specimens. To ensure a representative selection of the insulated iCFS, the iCFS had successfully completed the insulation test from Section 2.3.1. The cross-sectional analysis reveals that the insulation layer thickness varies between approximately 16 µm and 68 µm in the first two cross sections (Fig. 6a and b), whereas thicknesses of up to 133 µm are observed in Fig. 6c, representing a locally thick-walled region. In addition, microscopic voids are present between the first and second resin layers of the sensor, as most clearly visible in Fig. 6c. Since these voids are predominantly located around the sensor fibers, they are likely caused by entrapped air within the resin during the dip-coating process. In order to resolve this issue in the future, applying a vacuum after mixing the epoxy resin for the second insulation step could be helpful in reducing the amount of air in the resin. However, it is important to maintain a constant temperature during this process, as otherwise the viscosity properties necessary for uniform insulation may change.

To provide a qualitative impression of a sensor's outer surface, Fig. 7 shows insulated sensor fibers, including a thicker section in Fig. 7c, which cannot be entirely avoided during the manufacturing process but can be minimized by adjusting the resin viscosity through optimization of the ambient process temperature.

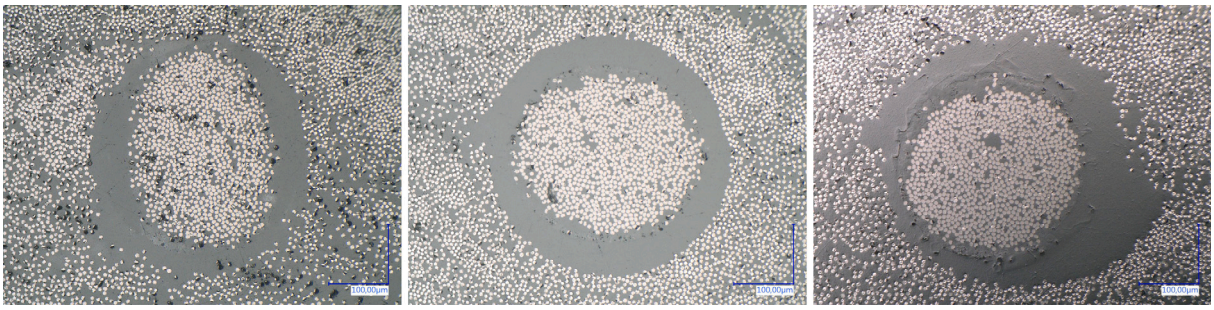
To determine the average amount of resin uptake, the FVC was determined as described in Section 2.2.1 after the first impregnation step and the insulation process using dip coating. Fig. 8 shows an average FVC of 49.8 % after the first impregnation layer. After dip coating, the average FVC of the impregnated CFS with an additional insulation layer is reduced to an average of 31.8 %. It should be noted that, due to the measurement procedure, locally thicker regions may result in decreased overall FVC values.

3.2. Integration of iCFS into composite laminates

To investigate the functionality and performance of the iCFS under controlled tensile loading conditions, the sensors were embedded in unidirectional CFRP and GFRP laminates and subjected to tensile testing. The sensor integration was designed to limit the integration impact by using a thin epoxy-based insulation layer compatible with the thermoset matrix and curing process. However, the effect of the embedded sensor on laminate stiffness, strength, and failure behavior was not quantified in this study.

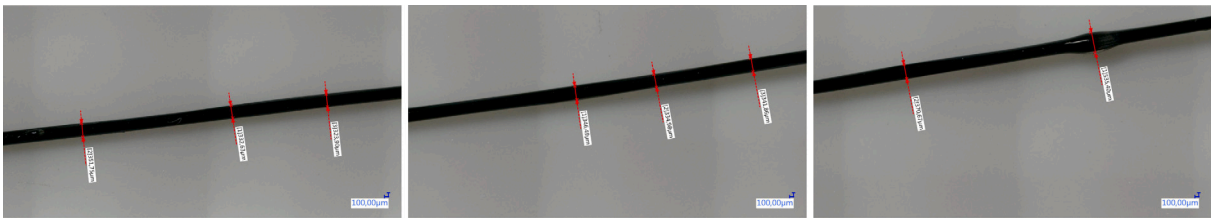
For this purpose, the pre-insulated iCFS was positioned at the mid-plane of the laminate stack. As shown in Fig. 9b and c, the sensors were embedded parallel to the fiber direction of the composite and routed such that the copper wires could exit the laminate without causing delamination or resin accumulation. The corresponding laminate structure was described in detail in Section 2.2.2 and illustrated in Fig. 4.

The positioning of the sensors and the soldered connections within the laminate required precise control of the prepreg layout and insulation of the wire exits using release foil. The integration approach ensured that both the sensor and its contacts were fully encapsulated within the thermoset matrix and ensured that the copper cables remained accessible for a subsequent connection to the measuring device.



(a) (b) (c)

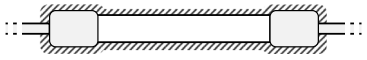
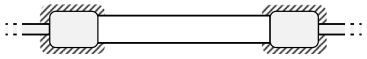
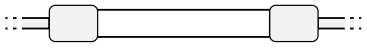
Fig. 6. Cross-sectional micrographs of iCFS embedded in pure epoxy resin. The insulation thickness ranges from approximately 16 µm to 52 µm in (a), as well as from 36 µm to 68 µm (b). (c) shows a thick-walled region with insulation thicknesses from 22 µm to 133 µm.



(a) (b) (c)

Fig. 7. (a) and (b) Ideally insulated sensor sections corresponding to the cross sections shown in Fig. 6a and b; (c) locally thicker sensor section corresponding to a possible cross section as shown in Fig. 6c.

Table 1
Comparison between the resistance of CFS before (R_0) and in a liquid gallium bath (R_{Ga}) for iCFS with full insulation, with insulated soldering joints only and without insulation layer. The insulation is illustrated with dashed lines. It shows that the one-layer-insulated fibers have general potential for insulation but appear to show imperfections that limit insulation quality. Every test was performed once with five specimens for each insulation type.

No.	Insulation type	R_0 (Ω)	R_{Ga} (Ω)	R_{Ga}/R_0 (%)
1		42.63 ± 0.44	42.54 ± 0.37	99.8 ± 0.02
2		43.67 ± 0.39	33.48 ± 3.70	76.6 ± 0.08
3		44.21 ± 0.46	1.03 ± 0.12	2.3 ± 0.02

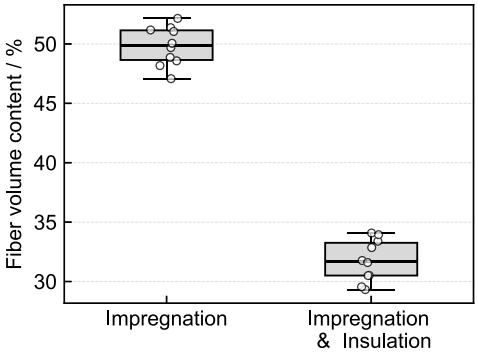


Fig. 8. Comparison of the FVC of twisted T300 carbon fibers with the first layer of resin impregnation and with an additional insulation layer.

3.3. Sensor insulation test in a conductive Ga bath

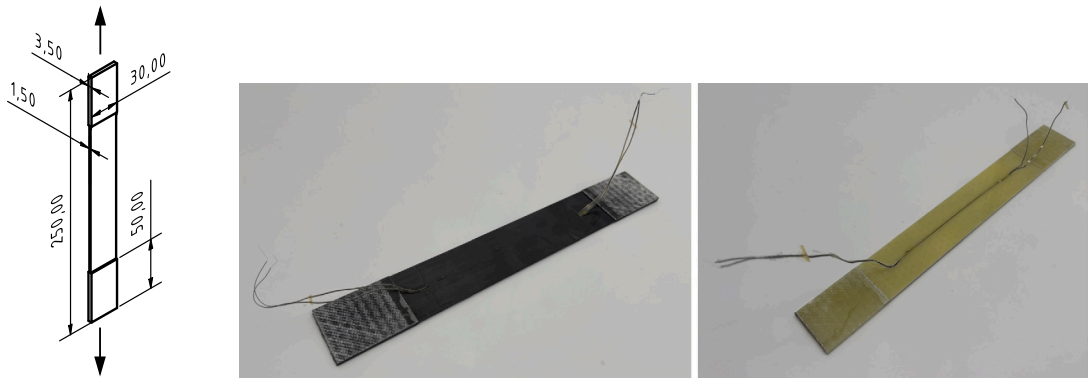
To evaluate the effectiveness of the applied insulation layer, a resistance comparison was performed by measuring the electrical resistance of the carbon fiber sensors in air (R_0) and after immersion in a bath of liquid gallium at 35°C (R_{Ga}). The test setup is illustrated in Fig. 5, and the corresponding measurement results are summarized in Table 1.

Uninsulated sensors (No. 3) exhibited a drastic reduction in resistance when immersed in the conductive gallium bath, indicating a direct electrical path through the gallium and insufficient electrical isolation under the investigated test conditions. Partially insulated sensors, with insulation applied only to the solder joints (No. 2), demonstrated some inherent electrical resistance due to surface wetting effects but still showed a significant drop in resistance, which indicates insufficient insulation of the sensor fiber itself.

In contrast, fully insulated sensors (No. 1) maintained over 99.8 % of their initial resistance, demonstrating effective electrical isolation of the sensor from the conductive gallium bath under the investigated test conditions. This result supports the suitability of the epoxy insulation concept for subsequent investigation of embedded iCFS in electrically conductive CFRP laminates.

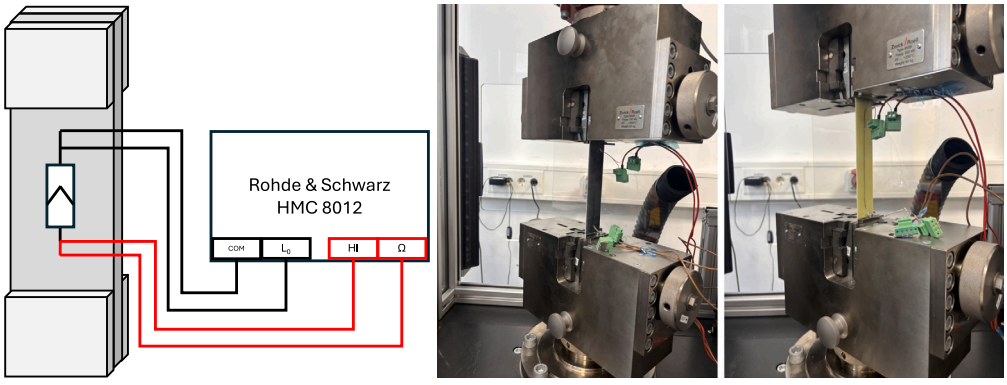
3.4. Piezoresistive properties of iCFS embedded in CFRP and GFRP determined by tensile testing

To assess the piezoresistive behavior and gauge factor of the insulated carbon fiber sensors (iCFS), tensile tests were conducted on



(a) (b) (c)

Fig. 9. Illustration of the test specimens: (a) drawing of the tensile specimens, (b) iCFS embedded in CFRP, (c) iCFS embedded in GFRP.



(a) (b) (c)

Fig. 10. (a) Wiring diagram of the tensile test with embedded iCFS. (b) Tensile test of an embedded iCFS in CFRP and (c) in GFRP for comparison of the sensor response in the two investigated laminate configurations.

unidirectional CFRP and GFRP specimens with embedded sensors (Fig. 9). The specimens were prepared in accordance with DIN EN 2561 with an increased sample width (Section 2.2.2) and tested in cyclic loading at two strain levels: 0.2 % and 0.6 %, which are reasonable strain levels for health monitoring for composite pressure vessels [41]. For each specimen and target strain level, five repeated measurements were conducted. Each measurement consisted of five consecutive loading–unloading cycles analyzed together using a single fit. This yielded five fitted gauge factors per specimen and strain level. The resulting 25 cycles represent repeated observations on the same embedded sensor and specimen rather than independent replicates. Strain was measured using a video extensometer, while the sensor response was recorded using a four-point resistance measurement setup (Fig. 10). After manual data matching, the gauge factors for the load cycles up to 0.2 % and 0.6 % strain were calculated according to Eq. (6), as exemplarily shown in Fig. 11 for one loading-unloading cycle.

The results of the cyclic loading tests with the embedded iCFS, presented in Table 2 and Fig. 12, show an approximately linear relationship between strain and resistance change for both CFRP and GFRP specimens. Within the limited specimen set, the sensor responses observed in CFRP and GFRP laminates were similar. The measured gauge factors were in a comparable range for both material types. The initial resistance values were in a similar range for both material systems, and the gauge factors at 0.2 % strain were closely grouped between 1.64 and 1.74. At 0.6 % strain, the gauge factors increased to values between 1.76 and 2.12. While most specimens showed only small changes between the two strain levels, one specimen in each material group exhibited a more pronounced increase. This indicates specimen-dependent variations in the sensor response, which may be related to

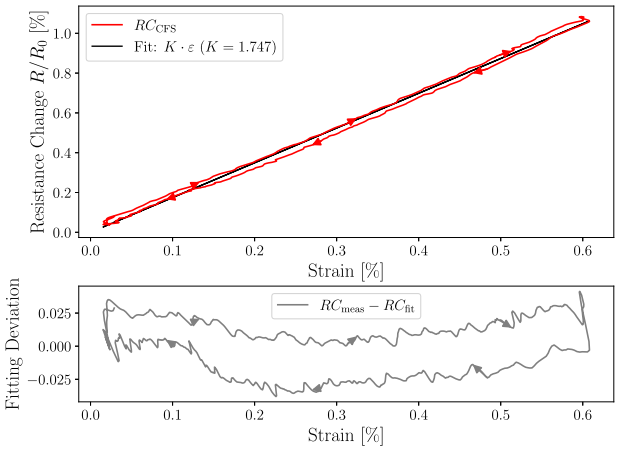


Fig. 11. Exemplary representation of one loading–unloading cycle from a five-cycle CFRP measurement used to determine the gauge factor by a single least-squares fit according to Eq. (6). The fit was calculated jointly from all five cycles, although only one cycle is shown for clarity. The arrows indicate the progression of loading and unloading. The lower panel shows the FD for each strain value. The deviation is largest in the intermediate strain range during unloading, whereas during loading, larger deviations occur near the lower and upper ends of the strain range.

local strain-transfer conditions, sensor embedding quality, or inconsistencies introduced during manual sensor fabrication. Furthermore, with

Table 2
Overview of the manufactured tensile specimens and tensile-test results for iCFS embedded in CFRP and GFRP. The comparable initial resistance values (R_0) of iCFS embedded in CFRP and GFRP are consistent with effective electrical isolation of the sensor in the investigated CFRP configuration. Comparing the gauge factors obtained at strain levels of 0.2 % ($k_{0.2\,\%}$) and 0.6 % ($k_{0.6\,\%}$) suggests an approximately linear resistance–strain relationship within the investigated strain range, although the limited dataset does not permit a definitive assessment of linearity. The gauge factors obtained for CFRP and GFRP are also comparable. Each gauge factor is reported as the mean ± sample standard deviation of five measurements on the same specimen, each comprising five jointly evaluated load–unload cycles. The sample standard deviation therefore characterizes the variability across the five measurements performed on the same specimen and does not characterize the reproducibility across independently manufactured sensors and specimens. A representative five-cycle measurement is shown in Fig. 12. Quantitative fit-quality metrics supporting the approximately linear relationship within the investigated strain range are provided in Table 3.

Material	No.	R_0 (Ω)	$k_{0.2\,\%}$	$k_{0.6\,\%}$
CFRP	1	41.542	1.72 ± 0.09	1.77 ± 0.06
	2	41.590	1.69 ± 0.05	2.12 ± 0.07
	3	41.794	1.74 ± 0.04	1.82 ± 0.04
GFRP	1	42.032	1.70 ± 0.03	1.86 ± 0.03
	2	41.777	1.71 ± 0.04	2.07 ± 0.03
	3	40.679	1.64 ± 0.08	1.76 ± 0.04

only three specimens per material system, the reproducibility across independently manufactured sensors and specimens cannot be conclusively assessed. The comparable responses observed for the CFRP and GFRP specimens are consistent with effective electrical isolation of the iCFS in the investigated CFRP configuration. However, the comparison does not isolate electrical conductivity as the only varying parameter, since the two laminate systems also differ in their reinforcement and resin systems.

The quantitative fit-quality and temporal-alignment sensitivity results are summarized in Table 3. The high R^2 values and low RMSE values support the approximately linear relationship between strain and relative resistance change within the investigated strain range. Furthermore, the low S_k values indicate that the fitted gauge factors are only weakly affected by additional relative time shifts within the investigated range of −0.5 s to +0.5 s.

The reported RMSE and R^2 values characterize the overall quality of the joint loading-unloading fit. A separate quantitative evaluation of loading-unloading hysteresis was not performed in the present study.

These findings support the feasibility of integrating iCFS into thermoset-based UD laminates and show strain-dependent resistance responses over 25 cycles across five measurements in the investigated specimens.

3.5. Strain capacity evaluation

The following strain-capacity evaluation is based on one CFRP and one GFRP specimen. Accordingly, the observations are limited to the investigated specimens, and their generalizability and mechanistic interpretation require validation using a larger specimen population in future studies.

Under increasing load, the embedded iCFS showed qualitatively similar strain-related responses in the CFRP and GFRP specimens shown in Fig. 13. Although the stresses differ due to the differences in strength between the CFRP and GFRP laminate, the sensor behavior is structured into three phases. Up to a strain level of 0.7 %, the iCFS shows an approximately linear resistance response compared to the strain data provided by the video extensometer and is in a reasonable range for health-monitoring application, such as composite pressure vessels [41]. In such applications, the circumferential or hoop strain is typically of particular interest, as it is directly related to the dominant stress state induced by internal pressure. Consequently, sensor integration along the circumferential fiber direction is highly relevant for in situ monitoring concepts. Similar application-oriented integration strategies have been demonstrated for composite pressure vessels using fiber Bragg grating sensors embedded in the first hoop layer [42]. In this context, the proposed iCFS approach may be investigated in the future as a potential approach for integrated strain sensing in CFRP pressure-vessel structures.

For the individual CFRP and GFRP specimens investigated, the resistance response becomes increasingly nonlinear above approximately 0.7 % strain and continues until signal loss occurs at approximately 1.3 % strain for the CFRP specimen and 1.5 % strain for the GFRP specimen. Within this range, the CFRP specimen exhibits an abrupt decrease in the strain measured by the video extensometer, accompanied by a corresponding change in the iCFS resistance signal, as shown in Fig. 13c. The change in the resistance signal may indicate the initiation of an interlaminar crack, resulting in localized strain relaxation. However, this interpretation is based only on the observed resistance response, as no full-field strain measurement was performed and no visible damage was observed at this stage. Therefore, this damage mechanism cannot be fully proven from the present measurements. The second phase is followed by signal loss. It is important to note that no return of the signal to its initial resistance was observed, indicating a distinct sensor response under overload conditions.

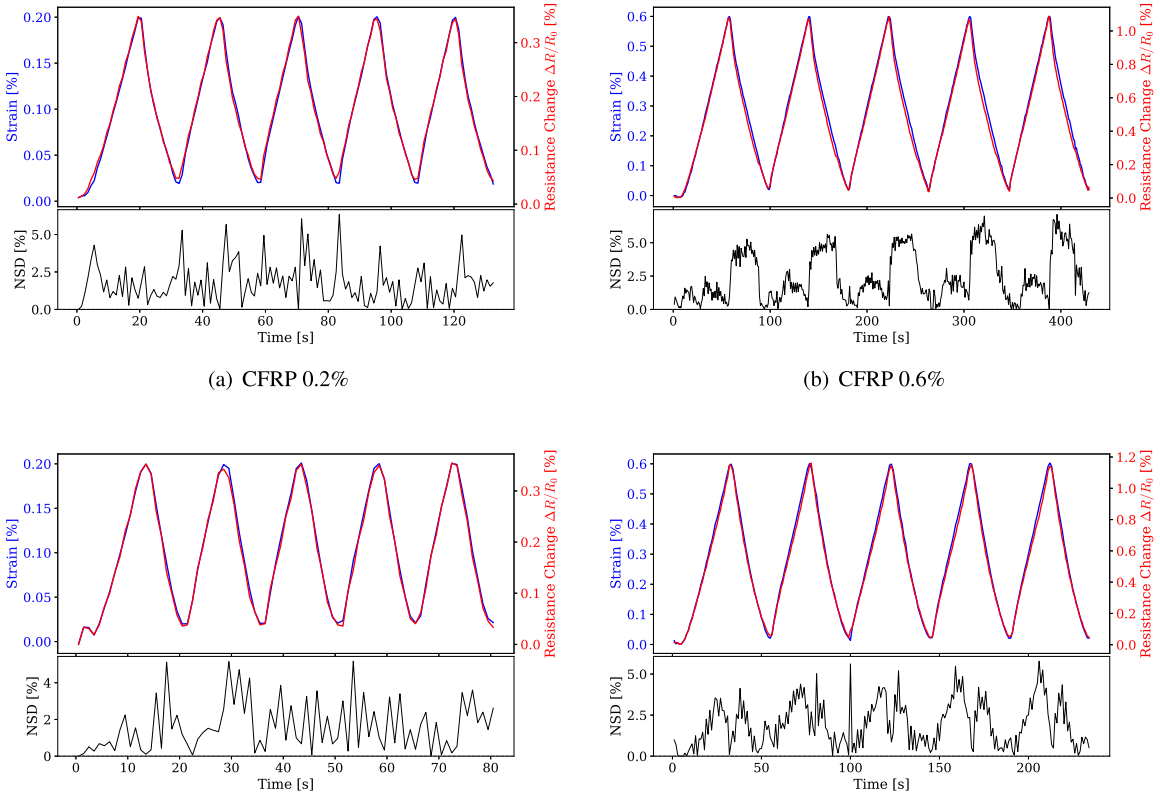
A possible explanation for the observed increase in nonlinearity at approximately 0.7 % strain is the onset of nonelastic behavior in the carbon-based sensor roving. A similar transition from linear elastic piezoresistive behavior was reported at approximately 0.7 % strain for non-embedded, PEKK-coated carbon nanoyarns [30]. However, because the sensor configuration and surrounding material differ from those investigated here, and the present observations are based on only one specimen per material system, this agreement should be regarded as a qualitative indication rather than confirmation of the underlying mechanism.

3.6. Sensor application based on composite architecture and load type

The present study demonstrates the feasibility of embedded iCFS for strain sensing in UD CFRP and GFRP tensile specimens under controlled room-temperature axial loading. This well-defined test configuration enables a focused evaluation of the electrical insulation concept and the strain-dependent piezoresistive response. Further validation is required to transfer the sensor concept to more complex laminate architectures, environmental conditions, and load cases, including long-term durability, structural-health-monitoring applications, pressure-vessel-related loading conditions, and the influence of the embedded sensor on laminate mechanical properties.

In multidirectional laminates, the sensor may be exposed not only to the nominal strain component in the principal loading direction, but also to transverse strain, in-plane shear, local bending, and complex strain gradients. In addition, the local laminate morphology can strongly affect the mechanical boundary conditions of the sensor. Ply crossovers, resin-rich regions, changes in local fiber volume content, and varying ply orientations may alter the strain-transfer conditions between the surrounding composite and the sensor. As a consequence, the measured sensor response may contain artifacts that are not directly related to the global structural strain state. Furthermore, local stress concentrations may increase the risk of sensor damage or sensor-induced damage initiation.

The orientation of the sensor relative to the principal loading direction is therefore expected to be particularly relevant. If the sensor is aligned parallel to the dominant strain direction, the measured response is likely governed primarily by axial strain transfer. In contrast, a transverse or inclined sensor orientation may introduce a stronger influence of transverse deformation, shear deformation, and possible local bending of the sensor. This may affect both the sensitivity and



(a) CFRP 0.2% (b) CFRP 0.6%

(c) GFRP 0.2% (d) GFRP 0.6%

Fig. 12. Overview of strain and relative resistance changes ($\Delta R/R_0$) of the iCFS embedded in CFRP and GFRP laminates under cyclic loading. Five loading cycles are shown for CFRP specimens up to (a) 0.2 % and (b) 0.6 % strain, and for GFRP specimens up to (c) 0.2 % and (d) 0.6 % strain. The lower panels show the normalized signal deviation (NSD) between the separately normalized strain and resistance-change signals, which is used to qualitatively visualize the temporal distribution of differences between the signal profiles rather than an absolute measurement error. The representative measurements show approximately proportional resistance responses over the five displayed cycles under the investigated conditions.

Table 3
Gauge factors, nominal fit quality, and sensitivity to temporal alignment for iCFS embedded in CFRP and GFRP. Each row summarizes five repeated measurements on the same specimen at the specified strain level. Each repeated measurement comprises five loading–unloading cycles evaluated jointly using a single least-squares fit. Gauge factors are reported as mean ± sample standard deviation across the five repeated measurements, characterizing within-specimen repeated-measurement variability. RMSE and centered R^2 at the nominal alignment are reported as mean [minimum–maximum] across these five measurements. For each repeated measurement, S_K is calculated as the maximum absolute relative change in gauge factor over additional time shifts ranging from −0.5 to +0.5 s in increments of 0.1 s. The five resulting S_K values are summarized as mean [maximum] and expressed in percent. RMSE is expressed in percentage points of relative resistance change.

Material	No.	Strain level (%)	k mean ± SD	RMSE (pp) mean [min–max]	R^2 mean [min–max]	S_K (%) mean [max]
CFRP	1	0.2	1.72 ± 0.09	0.009 [0.008–0.011]	0.991 [0.988–0.993]	0.33 [0.47]
CFRP	1	0.6	1.77 ± 0.06	0.027 [0.020–0.027]	0.992 [0.988-0.996]	0.11 [0.16]
CFRP	2	0.2	1.69 ± 0.05	0.010 [0.006–0.015]	0.988 [0.975–0.997]	0.54 [0.81]
CFRP	2	0.6	2.12 ± 0.07	0.043 [0.032–0.059]	0.984 [0.971–0.991]	0.08 [0.19]
CFRP	3	0.2	1.74 ± 0.04	0.010 [0.007–0.015]	0.989 [0.977–0.996]	0.52 [1.04]
CFRP	3	0.6	1.82 ± 0.04	0.015 [0.013–0.020]	0.985 [0.976–0.998]	0.24 [0.48]
GFRP	1	0.2	1.70 ± 0.03	0.007 [0.006–0.009]	0.995 [0.993–0.997]	0.62 [0.74]
GFRP	1	0.6	1.86 ± 0.03	0.016 [0.015–0.017]	0.998 [0.997–0.998]	0.12 [0.20]
GFRP	2	0.2	1.71 ± 0.04	0.008 [0.006–0.010]	0.994 [0.991–0.997]	0.54 [0.85]
GFRP	2	0.6	2.07 ± 0.03	0.029 [0.022–0.038]	0.994 [0.990–0.997]	0.16 [0.27]
GFRP	3	0.2	1.64 ± 0.08	0.014 [0.009–0.022]	0.977 [0.951–0.992]	0.66 [0.81]
GFRP	3	0.6	1.76 ± 0.04	0.023 [0.018–0.032]	0.995 [0.990–0.997]	0.10 [0.20]

the interpretation of the sensor signal. Therefore, the sensor response in complex laminates should not be assumed to be independent of the local fiber architecture or sensor orientation. It should also be noted that a single embedded iCFS primarily provides an orientation-dependent resistance response and does not intrinsically distinguish between axial, transverse, and shear deformation components. In complex multiaxial stress states, the measured signal represents the combined effect of the local deformation state, sensor orientation, and strain-transfer conditions. A separation of individual strain components would therefore require a defined sensor layout with multiple orientations, suitable calibration procedures, or additional reference measurements.

Filament-wound structures with pronounced crossing patterns represent a particularly relevant case for future investigations. Cross-ply regions generated during the winding process can contain a high density of fiber crossover points. These local geometric irregularities may lead to non-uniform compaction, resin-rich pockets, local waviness, and heterogeneous strain-transfer conditions. For an embedded sensor, such regions may cause local bending or transverse loading and may

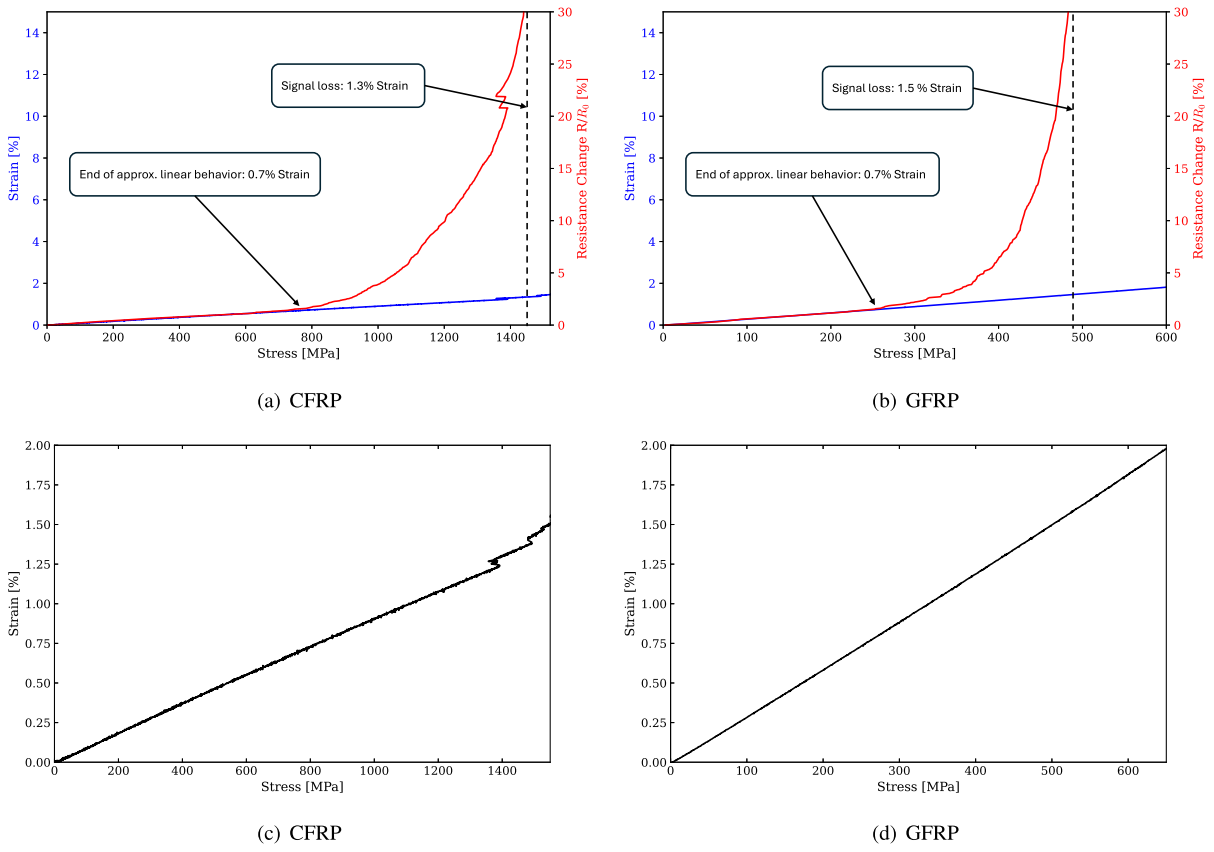


Fig. 13. iCFS resistance response and strain measured using a video extensometer for one CFRP specimen (a) and GFRP (b) sample under increasing tensile load. The iCFS measurement behavior can be divided into three phases. The first phase shows approximately linear behavior up to a strain level of 0.7 % in the one investigated CFRP and GFRP specimen each. The second phase is characterized by a nonlinear increase in the sensor signal until signal loss at 1.3 %/1.5 % (CFRP/GFRP), (c) a more detailed stress–strain diagram of the CFRP sample. At approximately 1400 MPa, the video extensometer recorded an abrupt decrease in the averaged axial strain, accompanied by a corresponding change in the iCFS resistance signal. This behavior may indicate the initiation of an interlaminar crack, resulting in localized strain relaxation. However, this interpretation cannot be confirmed based on the available measurements. (d) a more detailed stress–strain diagram of the GFRP sample.

therefore increase the probability of measurement artifacts or mechanical degradation of the sensor. For this reason, future tank-laminate experiments should aim to place the sensor within circumferential layers, for example between the +89° and -89° hoop-oriented plies. This positioning may reduce exposure to complex local loading conditions and provide a more defined strain-transfer environment.

Under compressive loading, the sensor response cannot yet be assumed to be directly equivalent to the tensile response. Although a monotonic and reversible resistance change may be expected as long as the sensor remains fully bonded to the surrounding matrix and the deformation remains elastic, compression introduces additional failure and signal-distortion mechanisms. These include local fiber or tow microbuckling, sensor waviness, interfacial debonding, and partial loss of strain transfer between the laminate and the sensor. Such effects may lead to non-monotonic or irreversible resistance changes and may promote premature delamination at or near the sensor interface. Therefore, the compressive sensing behavior must be validated separately before the sensor concept can be applied to compression-dominated load cases.

Bending loads may be less critical than compression if the sensor remains sufficiently bonded to the surrounding laminate and is not placed in regions with excessive strain gradients or local curvature. However, bending can still alter the local strain state at the sensor position, particularly in multidirectional laminates or near ply transitions. Therefore, the influence of bending on signal quality, strain transfer, and sensor durability should be examined in future work.

Further environmental and operational effects must also be considered for structural-health-monitoring applications. Thermal drift may influence the electrical resistance independently of mechanical strain and therefore requires temperature compensation or reference sensors. Moisture uptake may affect the sensor–matrix interface and the electrical stability of the embedded sensor. Pressure-vessel structures represent a potential future application, but their suitability has not been demonstrated in the present study. Such applications require additional validation under representative winding architectures, hoop and helical ply arrangements, pressure cycling, fatigue loading, multiaxial stress states, and relevant thermal conditions, including cryogenic cycling where applicable. Repeated cyclic loading may not only affect the composite structure itself, but may also induce sensor-specific fatigue mechanisms. Possible degradation processes include progressive debonding, changes in the sensor–matrix interface, accumulation of microdamage around the sensor, or fatigue-related changes in the sensor response. Consequently, the long-term stability, repeatability, and damage tolerance of the sensor under cyclic loading conditions must be assessed before its applicability to operational structural-health-monitoring scenarios can be fully evaluated.

4. Conclusion

This study presents a novel approach using thermoset-insulated carbon fiber sensors (iCFS) that enables strain measurements in CFRP laminates using a multi-layer epoxy-based insulation method. The proposed process enables electrically insulated sensor integration compatible with the investigated thermoset manufacturing process and

provides approximately proportional sensing behavior under cyclic tensile loading up to the investigated strain level of 0.6 %.

The insulation concept was evaluated by immersion tests in liquid gallium, in which fully insulated iCFS maintained over 99.8 % of their initial resistance, demonstrating effective electrical isolation from the conductive gallium bath under the investigated conditions. Partially insulated and uninsulated sensors showed substantial resistance drops upon immersion, indicating insufficient electrical isolation under these test conditions.

Further cyclic tensile tests of iCFS embedded in UD CFRP and GFRP laminates showed approximately proportional piezoresistive responses within the investigated strain range up to 0.6 %, with specimen-specific fitted gauge factors ranging from approximately 1.64 to 2.12. The strain-dependent resistance responses observed in the CFRP specimens, together with the comparable initial resistance values and fitted gauge factors obtained for the GFRP specimens, are consistent with effective electrical isolation of the iCFS in the investigated CFRP configuration. However, the comparison between the two material systems does not isolate electrical conductivity as the only varying parameter, since the CFRP and GFRP laminates also differ in their reinforcement and resin systems. Furthermore, with only three specimens per material system, the reproducibility across independently manufactured sensors and specimens cannot be conclusively assessed. Exploratory increasing-load tests performed on one specimen per material system revealed a distinct transition from an approximately proportional to a nonlinear resistance response, followed by signal loss at higher strain levels. These observations demonstrate that the iCFS exhibits a clearly identifiable response during progressive tensile loading. Further validation is required to associate these signal characteristics with specific overload or damage states and to assess their suitability for structural health monitoring.

These findings support the feasibility of the developed epoxy-based insulation and integration method for obtaining strain-dependent resistance responses from embedded iCFS in the investigated thermoset-based UD CFRP configuration with the sensor aligned in the 0° fiber direction under room-temperature axial tensile loading conditions. The approach therefore provides a basis for further investigation of integrated strain-sensing concepts, while its suitability for operational structural health monitoring has not yet been demonstrated.

Further work will include the investigation of insulation stability under thermal cycling and cryogenic conditions, as well as long-term durability under mechanical loading. Furthermore, the sensor performance will be investigated under more complex fiber orientations and loading scenarios. In addition, further investigations will focus on improving the insulation quality, reducing microscopic inclusions and defects within the insulation layer, and assessing the influence of the embedded sensor fibers on the strength and stiffness of the laminate.

CRediT authorship contribution statement

Maximilian Korff: Writing – original draft, Visualization, Validation, Software, Methodology, Investigation, Formal analysis, Data curation, Conceptualization. **Tobias Dickhut:** Writing – review & editing, Supervision, Resources, Project administration, Methodology, Funding acquisition.

Declaration of competing interest

The authors declare that they have no known competing financial interests or personal relationships that could have appeared to influence the work reported in this paper.

Acknowledgments

The authors are grateful to Yvonne Köppe-Kreißig from the Institute for Water Management of the University of the Bundeswehr Munich for supporting this study. We also acknowledge financial support for open-access publication by the University of the Bundeswehr Munich.

Data availability

Data will be made available on request.

References

[1] Olsson Robin, Cameron Christopher, Moreau Florence, Marklund Erik, Merzkirch Matthias, Pettersson Jocke. Design, manufacture, and cryogenic testing of a linerless composite tank for liquid hydrogen. Appl Compos Mater 2024;31(4):1131–54.
[2] Balageas Daniel, Fritzen Claus-Peter, Güemes Alfredo. Structural health monitoring. vol. 90, John Wiley & Sons; 2010.
[3] Horoschenkoff Alexander. Sensorelement für funktionelle faserverbundwerkstoffe. Light Des 2014;7(2):28–33.
[4] Xi Xiang, Chung DDL. Piezoelectric and piezoresistive behavior of unmodified carbon fiber. Carbon 2019;145:452–61.
[5] Balaji R, Sasikumar M. Graphene based strain and damage prediction system for polymer composites. Composites A 2017;103:48–59.
[6] Jovarauskaite G, Monastyreckis G, Mishnaevsky Jr L, Zeleniakiene D. Self-sensing composites with damage mapping using 3d carbon fibre grid. Composites B 2025;295:112182.
[7] Mikhalchan Anastasiia, Alvarez Angel Victor Labordet, Zarzoso Moises, Gonzalez Carlos, Vilatela Juan J. The effects of cnt type, alignment and dopants on piezoresistance in cnt fibres. Carbon 2025;232:119810.
[8] Christner Christian, Horoschenkoff Alexander, Rapp Helmut. Longitudinal and transverse strain sensitivity of embedded carbon fibre sensors. J Compos Mater 2013;47(2):155–67.
[9] Forintos N, Czigany T. Reinforcing carbon fibers as sensors: The effect of temperature and humidity. Composites A 2020;131:105819.
[10] Pérez-Aranda C, Rivero-Ayala M, Falla C, Gamboa F, Avilés F. Electrical monitoring of structural health of laminated composite panels under compressive loading using carbon nanotube yarns. Compos Commun 2025;102565.
[11] Mäder T, Nestler D, Wielage B. Strain sensing using single carbon fibres. In: Proceeding of the 18th international conference on composite materials. Jeju Island, Korea; 2011, p. 21–6.
[12] Sebastian James, Schehl Norman, Bouchard Michael, Boehle Matthew, Li Lingchuan, Lagounov Alexandre, Lafdi Khalid. Health monitoring of structural composites with embedded carbon nanotube coated glass fiber sensors. Carbon 2014;66:191–200.
[13] Rocha Helena, Semprimoschnig Christopher, Nunes João P. Sensors for process and structural health monitoring of aerospace composites: A review. Eng Struct 2021;237:112231.
[14] Ogi Keiji, Takao Yoshihiro. Characterization of piezoresistance behavior in a cfrp unidirectional laminate. Compos Sci Technol 2005;65(2):231–9.
[15] Wang Xiaojun, Chung DDL. Self-monitoring of fatigue damage and dynamic strain in carbon fiber polymer–matrix composite. Composites B 1998;29(1):63–73.
[16] Lee In Yong, Jang Juhyeong, Park Young-Bin. Advanced structural health monitoring in carbon fiber-reinforced plastic using real-time self-sensing data and convolutional neural network architectures. Mater Des 2022;224:111348.
[17] Jiang Xiaowei, Zhang Wenjin, Wang Xiaodong, Liu Ling. High deformation/damage localization accuracy of fibrous composites through deep-learning of single channel data from carbon nanotube sensors. Composites A 2024;187:108512.
[18] Scholle Patrick, Sinapius Michael. A review on the usage of continuous carbon fibers for piezoresistive self strain sensing fiber reinforced plastics. J Compos Sci 2021;5(4):96.
[19] Seiffert J, Bissinger M, Drechsler K. Integration of carbon fiber and fiber optical sensorsin continuous fiber-reinforced additivelymanufactured parts. In: ECCM21 proceedings, volume 3 - material and structural behaviour. 2024.
[20] Luan Congcong, Yao Xinhua, Shen Hongyao, Fu Jianzhong. Self-sensing of position-related loads in continuous carbon fibers-embedded 3d-printed polymer structures using electrical resistance measurement. Sensors 2018;18(4):994.
[21] Ye Wenguang, Dou Hao, Cheng Yunyong, Zhang Dinghua. Self-sensing properties of 3d printed continuous carbon fiber-reinforced pla/tpu honeycomb structures during cyclic compression. Mater Lett 2022;317:132077.
[22] Yao Xinhua, Luan Congcong, Zhang Deming, Lan Liujian, Fu Jianzhong. Evaluation of carbon fiber-embedded 3d printed structures for strengthening and structural-health monitoring. Mater Des 2017;114:424–32.
[23] Nam IW, Park Sol Moi, Lee Haeng-Ki, Zheng LJCS. Mechanical properties and piezoresistive sensing capabilities of frp composites incorporating cnt fibers. Compos Struct 2017;178:1–8.
[24] Can-Ortiz A, Abot JL, Avilés F. Electrical characterization of carbon-based fibers and their application for sensing relaxation-induced piezoresistivity in polymer composites. Carbon 2019;145:119–30.
[25] Salvado Rita, Lopes Catarina, Szojda Leszek, Araújo Pedro, Gorski Marcin, Velez Fernando José, Castro-Gomes João, Krzywon Rafal. Carbon fiber epoxy composites for both strengthening and health monitoring of structures. Sensors 2015;15(5):10753–70.

[26] Häntzsche E, Matthes A, Nocke A, Cherif Ch. Characteristics of carbon fiber based strain sensors for structural-health monitoring of textile-reinforced thermoplastic composites depending on the textile technological integration process. Sensors Actuators A 2013;203:189–203.
[27] Zestos Alexander G, Nguyen Michael D, Poe Brian L, Jacobs Christopher B, Venton B Jill. Epoxy insulated carbon fiber and carbon nanotube fiber microelectrodes. Sensors Actuators B 2013;182:652–8.
[28] Hasan MMB, Matthes A, Schneider P, Cherif Ch. Application of carbon filament (cf) for structural health monitoring of textile reinforced thermoplastic composites. Mater Technol 2011;26(3):128–34.
[29] Hasan Mir Mohammad Badrul, Nocke Andreas, Cherif Chokri. High temperature resistant insulated hybrid yarns for carbon fiber reinforced thermoplastic composites. J Appl Polym Sci 2013;130(2):1179–84.
[30] Zarzoso Moisés, Mikhalchan Anastasiia, Mocerino Davide, Romero-Rodriguez Pablo, Losada Ricardo, Vilatela Juan J, González Carlos. Strain sensing of structural composites by integrated piezoresistive cnt yarn sensors. Composites B 2024;286:111752.
[31] R&G Faserverbundwerkstoffe GmbH. Technisches datenblatt epoxidharz l20. 2022, härter eph 161.
[32] Big Difference GmbH & CoKG. Everglue 2k 5-minuten-epoxy epoxidharz. 2025, https://big-difference.com/everglue-2k-5-minuten-epoxy-200g?srsltid=AfmBOoqpZysbcL7XAuLivtzDPiVzR40D_eAlckj_mQy7pZ7C9pkqim31, [Accessed 03 May 2025].
[33] Hardianto Hardianto, Mey Gilbert De, Malengier Benny, Langenhove Lieva Van. Textile-based thermoelectric generator fabricated from carbon fibers. J Ind Text 2022;51(5_suppl):8411S–27S.
[34] Siau Sam, Vervaet Alfons, Degrande Siska, Schacht Etienne, Calster Andre Van. Dip coating of dielectric and solder mask epoxy polymer layers for build-up purposes. Appl Surf Sci 2005;245(1–4):353–68, Dip Coating.
[35] Müller Tobias. Kohlenstofffasern als piezoresistiver sensor zur dehnungsmessung und rissdetektion bei faserverbundwerkstoffen. VDI Verlag; 2014.
[36] Rude TJ, Strait Jr LH, Ruhala LA. Measurement of fiber density by helium pycnometry. J Compos Mater 2000;34(22):1948–58.
[37] DIN ENISO. 1183–1; kunststoffe—verfahren zur bestimmung der dichte von nicht verschäumten kunststoffen—teil 1: Eintauchverfahren, verfahren mit flüssigkeitspyknometer und titrationsverfahren. 2019.
[38] EN DIN. Din en 2561. Berlin, Germany: Deutsches Institut für Normung (DIN); 1995.
[39] VDI/VDE 2635. Experimental structural analysis - metallic bonded resistance strain gauges - characteristics and test conditions. 2024.
[40] Draper NR. Applied regression analysis. McGraw-Hill. Inc; 1998.
[41] Kang Huairong, He Pengfei, Zhang Cunman, Dai Ying, Lv Hong, Zhang Ming, Yang Donglin. Stress–strain and burst failure analysis of fiber wound composite material high-pressure vessel. Polym Polym Compos 2021;29(8):1291–303.
[42] Rocha Helena, Antunes Paulo, Lafont Ugo, Nunes Joao P. Processing and structural health monitoring of a composite overwrapped pressure vessel for hydrogen storage. Struct Health Monit 2024;23(4):2391–406.